Dynamics of Earth's bow shock under near-radial interplanetary magnetic field conditions

C. J. Pollock, L.-J. Chen, S. J. Schwartz, et al.

View Online   Export Citation   CrossMark

AIP Publishing

Dynamics of Earth's bow shock under near-radial interplanetary magnetic field conditions

View Online   Export Citation   CrossMark

C. J. Pollock,[1,a)] L.-J. Chen,[2] S. J. Schwartz,[3] S. Wang,[2,4] L. Avanov,[2,4] J. L. Burch,[5] D. J. Gershman, [2] B. L. Giles,[2] S. Raptis,[6] and C. T. Russell[7]

AFFILIATIONS

[1]Denali Scientific, Fairbanks, Alaska 99709, USA
[2]NASA/Goddard Space Flight Center, Greenbelt, Maryland 20771, USA
[3]University of Colorado LASP, Boulder, Colorado 80303, USA
[4]University of Maryland, College Park, Maryland 20742, USA
[5]Southwest Research Institute, San Antonio, Texas 78228, USA
[6]Division of Space and Plasma Physics, KTH Royal Institute of Technology, 114 28 Stockholm, Sweden
[7]University of California at Los Angeles EPSS, Los Angeles, California 90095, USA

Note: This paper is a part of the Special Collection: Plasma Physics from the Magnetospheric Multiscale Mission.
a)Author to whom correspondence should be addressed: craig@denaliscientific.org

ABSTRACT

We investigate the dynamics of Earth's quasi-parallel terrestrial bow shock based on measurements from the Magnetospheric MultiScale (MMS) spacecraft constellation during a period of near-radial interplanetary magnetic conditions, when the interplanetary magnetic field and the solar wind (SW) velocity are nearly anti-parallel. High-speed earthward ion flows with properties that are similar to those of the pristine SW are observed to be embedded within the magnetosheath-like plasma. These flows are accompanied by Interplanetary Magnetic Field (IMF) intensity of less than about 10 nT, compared to nearby magnetosheath intensities of generally greater than 10 nT. The high-speed flow intervals are bounded at their leading and trailing edges by intense fluxes of more energetic ions and large amplitude quasi-sinusoidal magnetic oscillations, similar to ultra-low frequency waves known to steepen and pileup on approach toward Earth to form the quasi-parallel bow shock. The MMS string-of-pearls configuration is aligned with the outbound trajectory and provides inter-spacecraft separations of several hundred km along its near 10^3 length, allowing sequential observation of the plasma and magnetic field signatures during the event by the four spacecraft. The SW-like interval is most distinct at the outer-most MMS-2 and sequentially less distinct at each of the trailing MMS spacecraft. We discuss the interpretation of this event alternatively as MMS having observed a quasi-rigid bow shock contraction/expansion cycle, ripples or undulations propagating on the bow shock surface, or a more spatially local evolution in the context of either a deeply deformed shock surface or a porous shock surface, as in the three-dimensional patchwork concept of the quasi-parallel bow shock, under the extant near-radial IMF condition.

I. INTRODUCTION

Earth's bow shock is formed upstream from Earth in the solar wind (SW) and is known from observation and theory to globally contract and expand in response to varying SW conditions, primarily the SW dynamic pressure and its associated magnetosonic Mach number M_{MS}, though the transverse IMF components (By and Bz in Geocentric Solar Ecliptic or GSE coordinates) and the upstream plasma beta (the ratio of plasma thermal pressure to magnetic pressure) are also known to influence its global location and shape [Chao *et al.* (2002) and references therein].

Earth's bow shock is also known to exhibit very different properties depending on the upstream magnetic field geometry. That geometry is characterized as either quasi-parallel (Qpar) or quasi-perpendicular (Qprp), a distinction based on whether the acute angle between the local upstream Interplanetary Magnetic Field (IMF) and the local normal (**n**) to the shock surface is larger (Qprp) or smaller (Qpar) than 45°. Wherever the bow shock location, in the Qprp case, it is characterized by a finite thickness that scales with the ion gyroradius based on the upstream magnetic field component parallel to the shock plane (Bale *et al.*, 2003). In the quasi-parallel case, this in-plane magnetic

component can become vanishingly small such that the shock thickness grows and becomes harder to define as both local and non-local instabilities and their impacts on the Qpar shock structure and dynamics come to dominate. A distinguishing characteristic of the Qpar bow shock vs the Qprp bow shock is that the Qpar bow shock is highly dynamic, re-forming in space and time under the influence of inflowing and steepening magnetic waves, while the Qprp bow shock is relatively quiescent, lacking the high-amplitude incident magnetic waves (Burgess, 1995). In the Qpar case, reflected ions can flow upstream along the IMF. These interact with the incoming SW to generate Ultra-Low Frequency (ULF) waves that propagate upstream in the SW frame of reference. However, the ULF wave speed is slow compared to that of the SW and the waves are ultimately convected back downstream toward the shock by the flow. The waves can steepen as they go, with some growing into Short Large Amplitude Magnetic Structures (SLAMSs; Lucek et al., 2008). The SLAMS cyclically disrupt the Qpar shock at their leading (downstream) edges and re-form it at their trailing (upstream) edges, as first demonstrated in the 1D hybrid simulations of Burgess (1989) and pileup near the nominal shock location, becoming in aggregate the quasi-parallel bow shock. Meanwhile, remnants of the original magnetic structures continue to convect downstream with shocked ions (Liu et al., 2021). Consideration of finite length scales of SLAMS transverse to the incoming flow evokes the conceptual model of the Qpar bow shock as a "patchwork of three-dimensional structures" envisioned in Fig. 1 of Schwartz and Burgess (1991).

Large magnetic component variations associated with compressive upstream waves, some of which evolve into SLAMS, induce large variations in the local magnetic shock-normal geometry, with scales similar to the transverse SLAMS scales. Large-amplitude (compared to the upstream ion inertial length, λ_i) transverse spatial structure in the Qpar bow shock has been observed in numerical simulations (e.g., Johlander et al., 2022; Karimabadi et al., 2014) and inferred from observations (Johlander et al., 2022). The graphics presented by Karimabadi et al. (2014) clearly demonstrate the distinctive role that the Qpar geometry plays in enabling large amplitude shock surface undulations. Krauss-Varban (2008) used large spatial scale hybrid simulations to demonstrate that, in the interplanetary shock context, upstream wave activity generated from non-local shock-emitted ions can convect back to an otherwise oblique shock surface, steepening as they go, and modify the local magnetic geometry, thus generating regions that are more-or-less oblique than nominal. Positive feedback owing to ion emission from the more Qpar regions enhances these, ultimately producing shock surface undulations with wavelength near $100 \, \lambda_i$ under the extant simulation conditions (Krauss-Varban, 2008). Shorter wavelength propagating ripples on the shock surface have been seen in the Qprp case, in both hybrid [e.g., Winske and Quest (1988) and Lowe and Burgess (2003)] and full-particle simulations (Krauss-Varban et al., 1995). Similar small-amplitude ripples have been inferred, also in the Qprp case, from multi-spacecraft observations (Johlander et al., 2016).

Magnetosheath jets are defined (Plaschke et al., 2018) to be ion jets observed downstream of the nominal bow shock, with enhanced dynamic pressure compared to local magnetosheath values. Magnetosheath jets are frequently observed [e.g., Hietala and Plaschke (2013), Plaschke et al. (2018), and references therein], most commonly under Qpar bow shock conditions. Magnetosheath jets have also

appeared in the Qpar region of global (Karimabadi et al., 2014) and local (Hao et al., 2016) 2D hybrid simulations. They penetrate beyond the nominal bow shock into the magnetosheath and at times through it to impact the magnetopause, inducing observable signatures in the ionosphere–thermosphere–magnetosphere system (Plaschke et al., 2018), though a recent simulation study by Tinoco-Arenas et al. (2022) has demonstrated that this is likely to be unusual except at very high Alfvén Mach numbers. Hietala and Plaschke (2013) have developed a model of a nominally fully parallel (**B**, **n** parallel) but dynamically "rippled" shock surface. The "rippling" presents temporal and spatial variations in the local magnetic shock normal angle at any point on the surface. Different local shock normal angles yield correspondingly different upstream/downstream dynamic pressure ratios as dictated by local satisfaction of the Rankine–Hugoniot jump conditions, potentially providing explanation for the observations of magnetosheath jets downstream of Earth's Qpar bow shock.

In this work, we report observations, under nearly radial IMF conditions, of a high-speed SW-like Earthward ion flow embedded in a magnetosheath time series observed by Magnetospheric MultiScale (MMS) and consider interpretations such as a large high-speed magnetosheath jet, a global bow shock contraction/expansion, passage through propagating surface ripple or undulation, or encounter with a volumetric interstitial element of three-dimensional patchwork of SLAMS. The high-speed ion flow is observed sequentially by the four MMS spacecraft distributed along its near10^3 km long string-of-pearls (SOPs) constellation aligned approximately parallel to the local nominal shock normal. Since both the SW flow and the IMF are nearly radial at the time, the MMS constellation also extended nearly parallel to these. In this extreme and highly dynamic magnetic shock geometry, multi-scale shock dynamics and structure might give rise to penetrating streams, or granularity in spatial structure, most of which (though perhaps not all) evanesce before reaching Earth's magnetopause. We examine the nature and timing of the observed ion and magnetic field signatures along the line of the MMS constellation, compare observed shock locations with the model of Chao et al. (2002), and discuss their interpretation in terms of bow shock configuration and dynamics.

II. DATA

The presented properties of the SW and IMF that are used to drive the Chao et al. (2002) shock model are obtained from the 1-min cadence OMNI database (available at https://omniweb.gsfc.nasa.gov) and include data from NASA's Advanced Composition Explorer (ACE) and wind, both resident at the L1 orbit approximately 235 Earth radii (R_E) upstream in the SW. All OMNI data in the database have been processed to account for the propagation delay from L1 to the sub-solar bow shock and are tagged with the predicted bow shock arrival time in what is known to be an imprecise (owing to the large distance between the L1 observation point and the Earth's bow shock) but useful prediction. The OMNI magnetic field data used originate from either the magnetometer (MAG; Smith et al., 1998) on ACE or the Magnetic Field Investigation (MFI; Lepping et al., 1995) on Wind, and the OMNI plasma ion data originate from either the Solar Electron Proton and Alpha Spectrometer (SWEPAM) (McComas et al., 1998) on ACE or the Solar Wind Experiment (SWE) (Ogilvie et al., 1995) on wind. The OMNI L1 observations are augmented with observations from the Flux Gate Magnetometer (FGM) (Auster et al., 2008) and the Electrostatic Analyzer (ESA) (McFadden

et al., 2008) on THEMIS-B (ARTEMIS) (Angelopoulos, 2011) in cis-lunar orbit, 58 R_E distant on Earth's dusk side near (4, 58, −5) R_E in GSE coordinates during the time of interest. Observations near Earth are obtained from the MMS (Burch *et al.,* 2016) mission, from which ephemeris and science data are used. MMS magnetic field measurements are from the fluxgate magnetometer (Russell *et al.,* 2016), part of the MMS fields suite (Torbert *et al.,* 2016). MMS ion observations are from the Dual Ion Sensor (DIS), part of the Fast Plasma Investigation (FPI) (Pollock *et al.,* 2016).

III. OBSERVATIONS AND RESULTS

The time interval of interest is during the UTC afternoon of 12 February 2019. During this interval, the MMS constellation is on an outbound trajectory through the 0900 Magnetic Local Time magnetosheath in a String-of-Pearls (SOP) configuration. The order of flight along this line is MMS2, 1, 4, 3 with MMS2 in the lead. Distances between (MMS2–1, MMS1–4, MMS4–3) are (283, 236, 369) km. The line joining the four spacecraft approximates the GSE unit vector (0.92, 0.25, 0.29), which forms a 23° angle with the +x_{GSE} unit vector.

Figure 1 presents an overview of the interval in question: 14:00–15:30 UTC. Earth's magnetospheric system responds to the upstream SW and magnetic environment that is illustrated with OMNI L1 magnetic field data in Fig. 1(g) and parameters derived from OMNI L1 magnetic field and ion plasma data in Fig. 1(h). Upstream, the interval begins with the IMF almost purely in the −y_{GSE} direction (near −6 nT) until a transition occurs near 1420 (vertical line 1), when IMF Bx grows from near 0 to near 6 nT, where it remains for most of the rest of the interval. Both IMF By and IMF Bz also change at that time, achieving and maintaining magnitudes of 2–3 nT (IMF By becoming less negative and IMF Bz more positive). The situation remains thus until near 14:35 UTC (vertical line 2), when the IMF begins a more gradual change, with IMF Bx growing and both IMF By and IMF Bz decreasing in magnitude to less than 1 nT by 14:47 UTC. Neither component exceeds about 1 nT in magnitude through the rest of the interval. Thus, from 14:47 UTC onward, this interval is characterized by an IMF cone angle in GSE of less than about 13°, with excursions to much smaller values, particularly during the interval surrounding vertical line 3 at 15:00 UTC. The magnetic observations shown in Fig. 1(g) are consistent with ARTEMIS FGM observations (not shown) obtained concurrently near (4, 58, −5) R_E GSE. Derived upstream parameters at L1 are shown in Fig. 1(h), where the Alfvén Mach number (M_A) appears at the top, the magnetosonic Mach number (M_{MS}) is shown below that, the ratio of plasma thermal to magnetic pressure (beta) is in the second line from the bottom and twice (for readability) the SW dynamic pressure ($2m_p n_{iSW} V_{iSW}^2$ = 2Pdyn, where m_p is the proton mass, and n_{iSW} and V_{iSW} are the measured SW density and bulk velocity) appears at the bottom in units of nP. These upstream quantities are quite steady during the entire interval shown in Fig. 1: M_{MS} = 5.15 ± 0.20 and Pdyn = 2.19 ± 0.22 nP (citing mean, maxima and minima) throughout the interval presented. Thus, among the upstream parameters (P_{dyn}, M_{ms}) that are known to control the magnetopause and bow shock boundary location, very little variation is evident.

The top four panels in Fig. 1 display data from the leading MMS2 probe within Earth's magnetosheath: (a) GSE magnetic field components and magnitude, (b) DIS ion E/q-t energy flux spectrogram, (c) DIS ion bulk velocity, and (d) DIS ion density. The next two

panels display derived parameters, including (e) the magnetosheath ion ram pressure ($m_p n_{iSH} V_{iSH}^2$), where m_p is the proton mass and n_{iSH} and V_{iSH} are the measured magnetosheath density and bulk velocity) and (f) the ion flow cone angle [$\cos^{-1}(-V_{ix}/|V_i|)$], providing a measure of the level of deflection from the nominal SW flow direction. Note that we have assumed all ions are protons. Upstream IMF changes [Fig. 1(g)] are reflected in the magnetic and ion signatures in the magnetosheath shown in Figs. 1(a)–1(f). Positive growth in all three magnetosheath magnetic field components is observed to nearly coincide just before 14:20 UTC with the growth and rotation observed in the IMF [Fig. 1(g)] at that time, as are large increases in their variability that are not seen in the IMF. That variability increases even further beginning shortly after 1435 (vertical line 2) when IMF By and Bz begin their concurrent decreases in magnitude while IMF Bx remains large until and beyond MMS' final passage through the bow shock into the SW at 15:19:35 UTC (vertical line 4).

Magnetosheath ion spectra [Fig. 1(b)] show qualitative changes driven by the IMF. Near 14:17 UTC (vertical line 1) the flux briefly intensifies at a few hundred eV and is depleted at energies above 1 keV, after which ion bulk parameters [Figs. 1(c)–1(e)] increase and become more variable. At the same time, the flux of higher energy (10 keV) ions increases and remains elevated (with intermittent decreases) through the rest of the interval. Thus, the properties of the magnetosheath become typical of those behind a Qpar shock after the IMF change from negative By dominant to Bx dominant seen in Fig. 1(g). The nature of observed ion fluxes in Fig. 1(b) again changes near 14:40 UTC (vertical line 2), where the E/q spectra become more narrow and appear more variable, exhibiting larger peak fluxes and mean E/q. These changes are also reflected in both increased values and variability of bulk velocity [Fig. 1(c)] and ram pressure [Fig. 1(e)]. Note that the average density [Fig. 1(d)] does not change much at this time but becomes much more variable. The ion velocity cone angle [Fig. 1(f)] is mainly oblique through the interval (near 30°–40°), as the magnetosheath flow is deflected around the obstacle. There is an interesting cyclic variation in the angle with a near 3 min period between 14:20 UTC (just after the interplanetary turning) and 14:40 UTC when the IMF begins to become more radial. After that, the cone angle is generally smaller and has numerous brief excursions toward zero, the most prominent of which, near 14:57 UTC, is discussed below.

In Fig. 1, vertical line 3 is placed at 14:55 UTC, just to the left of the event that is used to illustrate the key message of this paper. The event is evident in Fig. 1, panels (b)–(f). A distinct narrowing of the spectrum of ion energy flux vs E/q [Fig. 1(b)]; a bipolar signature in the ion bulk speed starting from near 200 km/s, peaking near 330 km/s and then minimizing near 100 km/s before returning to baseline [Fig. 1(c)]; the ion density goes through a deep minimum (5–10 cm^{-3}), exhibiting the lowest values seen through this pass and surrounded by two narrow spikes to values comparable to the highest densities seen throughout the interval [Fig. 1(d)], yielding a dynamic pressure [Fig. 1(e)] that is also reduced through the event. Finally, a deep depression in the ion speed cone angle to near zero is observed [Fig. 1(f)]. Notably, this event occurs during the interval [Fig. 1(g)] when both IMF By and Bz components near Earth are very close to zero; i.e., the IMF at Earth is nearly radial.

Figure 2 shows details of the event during the 3-min interval from 14:56:00 UTC to 14:59:00 UTC for all four MMS spacecraft on the order of their outbound flight. We show MMS FGM magnetic field
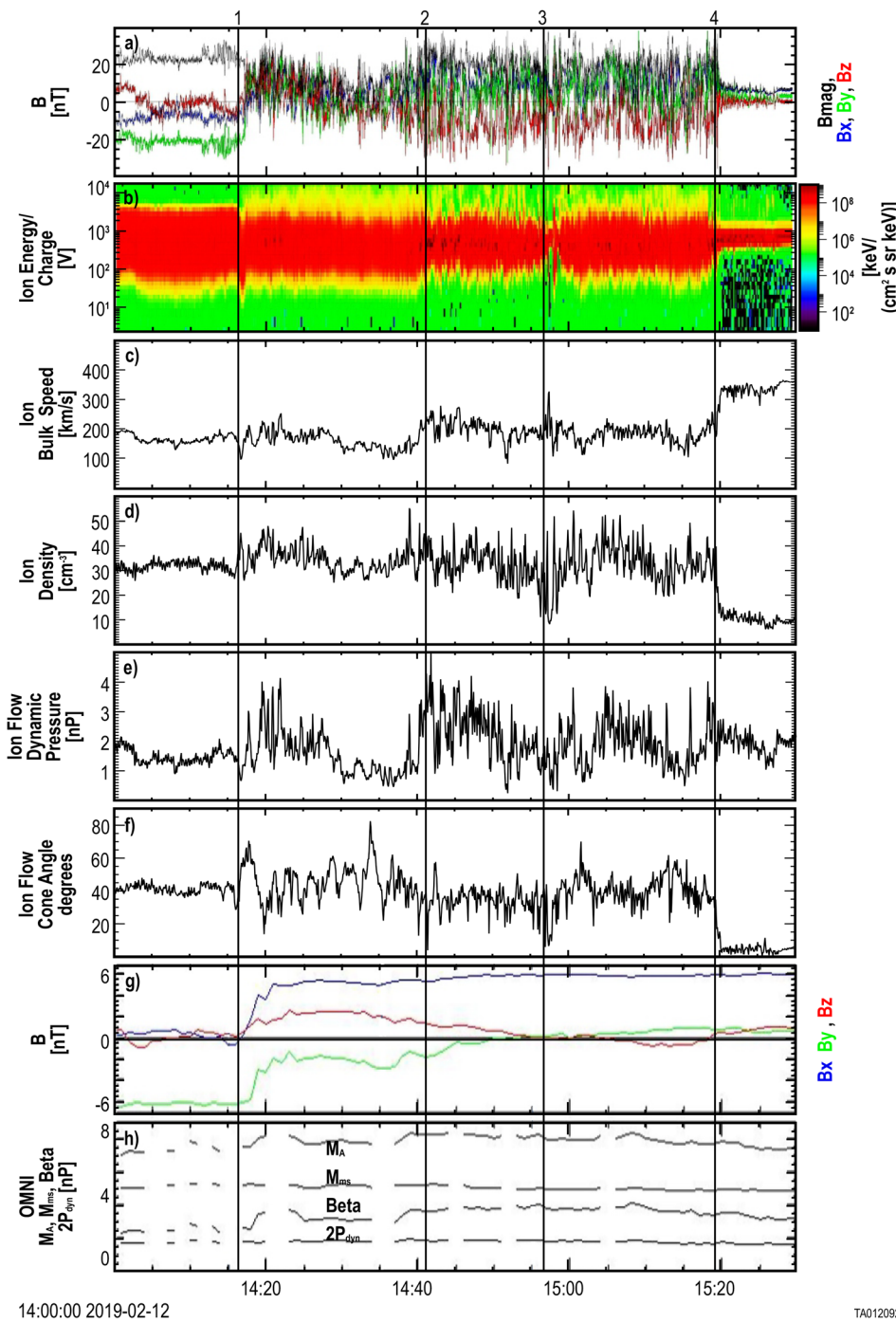
FIG. 1. An overview of an MMS outbound flight through the pre-noon terrestrial magnetosheath and relevant upstream drivers during the 1.5-h interval extending from 14:00 to 15:30 UTC on 12 February 2019. Panels (a)–(f) are from MMS-2 at fast survey cadence (62.5 ms for B-field and 4.5 s for ions) while panels (g) and (h) are OMNI data at a 1-min cadence. From top to bottom are shown (a) GSE magnetic field components and magnitude, (b) ion energy flux plotted with logarithmic color code in energy/charge-time format, (c) ion bulk speed, (d) ion density, (e) ion dynamic pressure: $m_p n_i V_i^2$, where m_p is the proton mass and n_i and V_i are the measured solar wind number density and bulk flow speed, and (f) the angle between the ion velocity and the negative GSE x-axis. We have assumed all measured ions are protons. Upstream values shown include (g) three GSE components of the IMF and (h) Alfvén Mach number at the top, magnetosonic Mach number below that, the ratio of plasma thermal to magnetic field pressure (beta) at second from bottom and 2× the solar wind dynamic pressure ($2\,mnV^2$) at the bottom. Vertical lines are placed near times of note as described in the text.

components (Bx in blue, By in green, and Bz in red) and magnitude (black) in Fig. 2, Panels (a), (c), (e), and (g), at 62.5 ms cadence and ion E/q-t spectrograms focused on ions moving in the $-x_{GSE}$ (anti-sunward) direction in Fig. 2, panels (b), (d), (f), and (h). The plots are arranged in four pairs from top to bottom representing the four MMS spacecraft in-flight order (MMS2, MMS1, MMS4, and MMS3).

The vertical axes on the magnetic field plots are identical (±40 nT), as are those for the ion E/q (0.002–18 keV/q) and the logarithmic color scales for the ion energy flux. Common to all four spacecraft are qualitative features in the magnetic and ion signatures that are most pronounced at the leading spacecraft (MMS2) and progressively less pronounced at MMS1, MMS4, and MMS3 that trail MMS2 by 283,
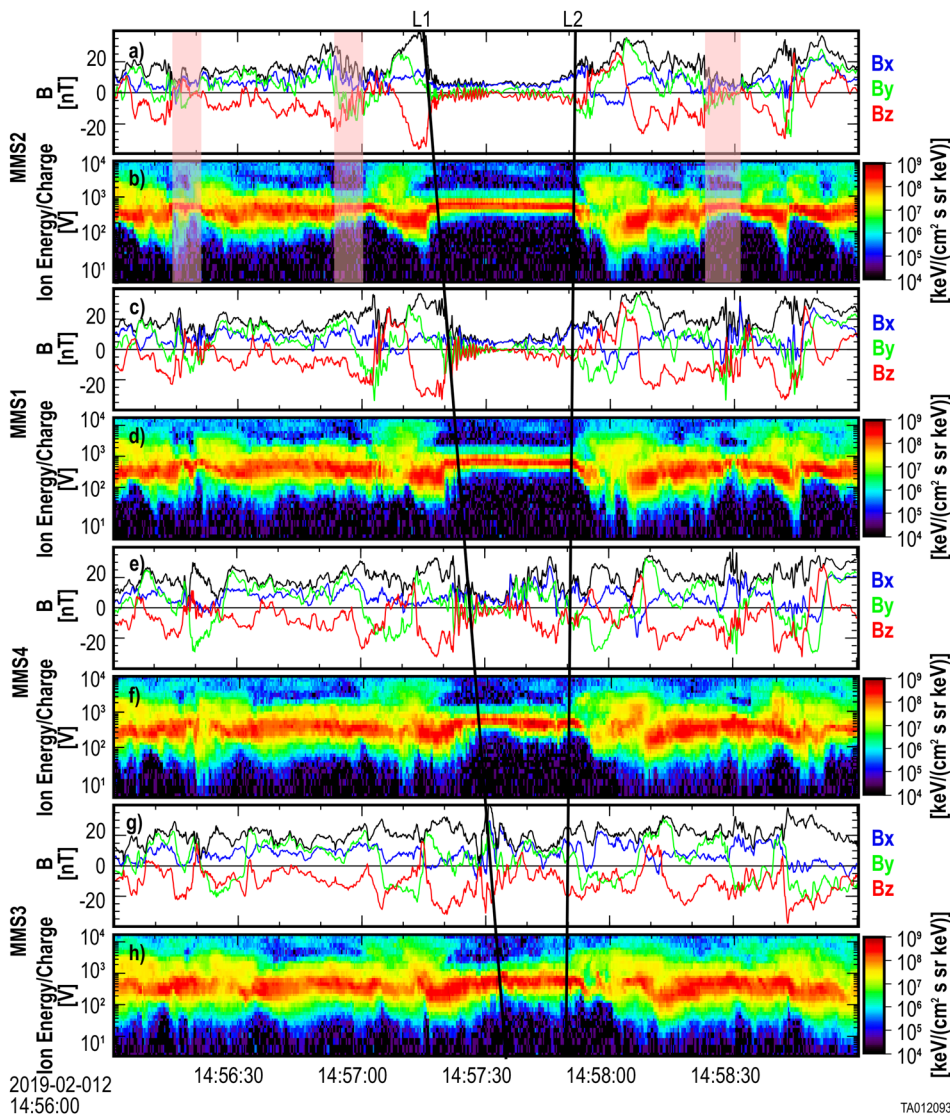
FIG. 2. MMS2 (a) and (b), MMS1 (c) and (d), MMS4 (e) and (f), and MMS3 (g) and (h) magnetic field and ion observations are presented during the 3-min interval from 14:56:00 to 14:59:00 UTC 12 February 2019. For each of the four spacecraft, from top to bottom are shown (a), (c), (e), and (g): GSE magnetic field components (Bx: blue; By: green; Bz: red) and magnitude (black) at 62.5 ms cadence; (b), (d), (f), and (h): ion E/q-t spectrogram for ions moving anti-sunward at 150 ms cadence. The two lines (L1) and (L2) are drawn by inspection to align with (L1): sequential precipitous decreases in |**B**| at MMS2 and MMS1 near 14:57:30 UTC and (L2): nearly concurrent decreases in the energy of peak flux at MMS1 and MMS2 near 14:57:50 UTC.

519, and 888 km at this time. At MMS3 the signatures are difficult to pick out and are arguably not present, though the ion flux signatures are more localized in E/q during the interval at MMS3 than during earlier and later intervals shown in Fig. 2(h).

The magnetic field at all four spacecraft shows irregular variations between less than 10 up to 30 nT through much of the interval shown. The most evident magnetic features of interest are the sustained field minima observed near the center of the interval, primarily at MMS2 and MMS1 though a vestige is seen at MMS4. These minima at MMS2 and MMS1 are bounded at their leading and trailing edges by strong field enhancements that are associated in each case with an approximate single cycle of large amplitude ULF near-circularly polarized By and Bz component fluctuation in which Bz leads By in phase in the spacecraft frame. This is much like the case of ULF waves often observed at the upstream edge of the Qpar bow shock and that are the

major elements of SLAMS. At MMS2 near 14:57:15 UTC, the magnetic intensity decreases to small values and a small amplitude higher frequency wave train ensues. These higher frequency waves correspond to whistler waves typically associated with the evolution of SLAMS at the Qpar bow shock (Schwartz *et al.*, 1992). They decay away by 14:58:30 UTC, near the center of the period of reduced field strength, before interestingly re-appearing at a somewhat lower frequency than previously until near 14:58:55 UTC, when the magnetic intensity recovers similar magnitude to that before 14:58:15 UTC and another approximate single cycle ULF fluctuation in By and Bz is observed. Similar magnetic features to those described above at MMS2 are seen at MMS1. At MMS4, next in line, the features are far less clear and at the trailing MMS3, they are essentially unrecognizable.

The sloped line labeled L1 in Fig. 2 at the leading edge of the event is placed by the eye to align with large decreases in |**B**| seen at

MMS2 and MMS1. Extension of this line to MMS4 and MMS3 passes very close to large decreases in |**B**| at both locations. The line's purpose is to illustrate dispersion in the leading-edge signatures of the observed B-field depression among the four spacecraft, which implies propagation along the line of the constellation. The plausibility of propagation speed near 102 km/s across the entire constellation is established by the fact that L1 lines up nicely with prominent magnetic depressions at both MMS4 and MMS 3, which observed its lowest field values through the event at that time. We return to the topic of relative signature timing below and in supplementary material S1.

Between 14:57:15 UTC and 14:57:50 UTC, concurrent with the sustained magnetic field minimum described above, the ion energy fluxes at MMS2, MMS1, and MMS4 take on different characteristics from those seen during most of the rest of the interval, becoming strongly peaked in E/q near 1 keV/q. Like the magnetic observations, this ion signature is most clear and persistent at MMS2 and progressively less so at MMS1, MMS4, and MMS3 where the signature is arguably not present. The magnetic and ion flux signatures within this interval look very much like those of the pristine SW, particularly at the leading MMS2 and MMS1 spacecraft. This interval of SW-like plasma is also bounded at earlier and later times by populations of more energetic particles that must have arisen from the SW interaction with the shock region, undergoing reflection and heating before ultimately returning to the boundary region. The onset of these particles at 14:57:00 is observed at all four MMS observatories and, unlike the onset of the high-speed ion flow shortly thereafter, is not dispersed in time across the MMS constellation. The more energetic particles then disappear at each spacecraft before the appearance of the high-speed flow.

The sloped line (L1) on the left in Fig. 2, drawn based on |**B**| as described above, demonstrates that the dispersion in the onset of the high-speed ion flow at the leading edge of this event is similar to that in |**B**| in the case of MMS2 and MMS1, though this is not as clearly evident in the cases of MMS4 and MMS3, where a more gradual evolution in the ion flux is observed at this time. A second line (L2) is placed on Fig. 2 near 14:57:52 UTC, where there is a break in the ion E/q spectrograms, with the energy of peak fluxes sharply decreasing at all four spacecraft, signaling the end of the SW-like interval. The feature is most clearly visible at MMS2, MMS1, and MMS3. The line L2 is drawn vertically, based on the time of the break in the ion flux signatures, in contrast with delays implied by slanted line L1 among the four spacecraft. Analysis of the timing (see supplementary material, S-1) in this trailing-edge ion–flux transition shows that it occurs nearly simultaneously (to within less than 1 s) among the four spacecraft.

Incidentally, there are three other intervals during the 3 min shown in Fig. 2 where similar though much less pronounced SW-like ion flow characteristics are observed, notably at MMS2 near 14:56:20, 14:57:00, and 14:58:30 UTC. These three intervals are highlighted in semi-transparent color in Figs. 2(a) and 2(b). Corresponding signatures at these times, if present, are hard to pick out at MMS1 and not evident at all at MMS4 or MMS3. Having noted these more minor and apparently less deeply penetrating examples in our time sample, we focus for the remainder of this work on the prominent event beginning near 14:57:15 UTC.

Figure 3 shows processed versions of the GSEy and GSEz magnetic components measured at each spacecraft: (a) MMS2, (b) MMS1, (c) MMS4, and (d) MMS3. In each case, the component data have
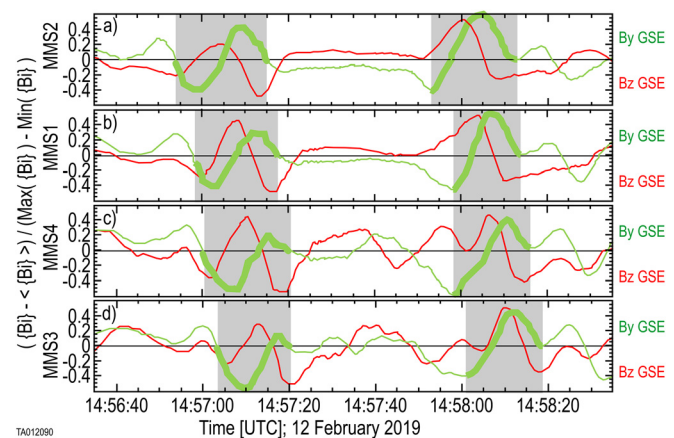

FIG. 3. Representations of the fast survey rate GSE By magnetic components measured at (a) MMS2, (b) MMS1, (c) MMS4, and (d) MMS3. For each panel, data have been smoothed over a 6 s window, had its mean value subtracted, and have been normalized to the difference between the maximum and minimum of the smoothed and mean-subtracted values. In the y-axis label "⟨Bi⟩" indicates the mean value of By or Bz and (Bi) indicates a 6-s smoothed By or Bz.

been smoothed (6 s window), had its mean value in the interval subtracted, and have been normalized to its maximum peak-to-peak amplitude within the interval, in that order. Figure 3 effectively illustrates the coherence of the lowest frequency magnetic signatures, particularly at the leading spacecraft, and the similarity in these signatures across spacecraft, especially at the leading and trailing edges of the SW-like flow seen most prominently at the leading MMS2 and MMS1.

The gray boxes in Fig. 3 highlight near-complete quasi-cycles of the GSE By component, whose line thickness has been enhanced within them for clarity. These highlighted quasi-cycles execute a full 2π, from one to the next up-going zero crossing at the leading edge and from one minimum to the next in the trailing edge where the simple sinusoid is less clear. We attempted two-parameter (frequency and phase) least squares fitting of single-cycle sin functions to the smoothed and normalized data to derive quantitative timing for these cyclic B-field component variations. We also fit Gaussian peaks and troughs to the extremities of the smoothed and normalized data to uniformly estimate the times of the minima and maxima of the By and Bz signatures. Neither the sinusoidal fitting of the wave form nor the Gaussian peak fitting near the extrema yield highly precise results with respect to the timing of the targeted long-period (15–20 s) magnetic undulations highlighted in Fig. 3. In the former case, the data depart substantially from a simple sinusoid over the approximate 15–20 s period in ways that differ from spacecraft to spacecraft. These departures indicate the space-time evolution of the target waveform and the presence of other evolving waves at various amplitudes, scales, and propagation characteristics superposed on the target waveform. The peaked Gaussian fits to the extrema, while providing better fidelity to the data used, are based only on data very local to the extrema and are also affected by evolution and wave admixture. Nevertheless, the peak fitting provides a systematic and consistent approach comparing the waveform extrema across the MMS constellation. For this purpose,

the smoothed data are normalized to the range (0, 1) for the peaks and (−1, 0) for the troughs. Near each peak or trough, all smoothed and normalized points with absolute value greater than 0.9 are included in a three-parameter least squares fitting procedure using the peaked functional form,

$$y = y_0 e^{\left(-\frac{t-t_0}{\Delta}\right)^2}, \qquad (1)$$

where among the fitted parameters y_0 represents the amplitude of the peak or trough, t_0 represents the peak or trough center location in time, and Δ estimates its temporal width. The fitted values of t_0 are extracted and combined with known spacecraft separations to yield feature propagation speeds along the line of the MMS constellation. The results are consistent with our *ad hoc* estimates of the relative timing represented by L1 in Fig. 2 and yield 96 ± 33 km/s at the leading event edge and 107 ± 29 km/s at the trailing edge (both anti-sunward). These are identical results, given the methodology applied. It is worth noting that the widths of the hand-drawn semi-transparent gray boxes in Fig. 3 are very uniform across the four spacecraft (MMS1: 57 s, MMS1: 59 s, MMS4: 57 s, and MMS3: 58 s).

We address the questions of where we expect the bow shock to be located and how variable that location is expected to be at the time in question using OMNI data both from L1 (235 R_E upstream) and from THEMIS-B in cis-lunar orbit (58 R_E away near 1800 magnetic local time) to drive the Chao (2002; hereafter C02) bow shock model and for comparison, the model of Jelinek *et al.* (2012; hereafter J12). Required C02 model inputs are the SW dynamic pressure, signed IMF B_z component, plasma beta, and magnetosonic Mach number. In the case of the THEMIS-B OMNI data, neither the electron temperature nor the Mach number is available. Therefore, we use the average magnetosonic Mach number obtained during the interval at L1 as a proxy

in the THEMIS-B driving parameters. The J12 model requires only the solar wind dynamic pressure as input. Results are shown in Fig. 4 where the raw C02 (panel a) model predicts the bow shock radial location to be near 17 R_E, for both the L1 and THEMIS-B driving parameters, fully 17% further from Earth-center than the value (R_F) finally observed at 15:19:20 UTC by MMS2 near 14.6 R_E (the large green dot at said coordinates in Fig. 4). Results from the simpler J12 model, displayed in panel (b): (1) predict the bow shock location to be significantly closer to the point where it was actually observed near 15:20 UTC than does the C02 model, (2) display significantly more variability in the shock location during the interval than predicted by the C02 model, (3) display a temporal trend that is less linear than that seen in the C02 model, and (4) owing to the latter two factors, display significantly more scatter around the linear fit to the temporal trend than does the C02 model. Finally, the J12 model shows a larger difference between the bow shock location predicted based on the L1 vs THEMIS-B parameters (1 R_E) than does the C02 model.

In all four cases (C02/L1, C02/THEMIS-B, J12/L1, and J12/THEMIS-B), we normalize the model shock distance (R_M) to the observation, multiplying by the ratio of the observed to model results at the time of final crossing,

$$R_{MN} = R_M \frac{R_F}{R_{MF}}, \qquad (2)$$

where R_F is the geocentric distance to the final observed shock-crossing and R_{MF} is the geocentric distance to the model-predicted shock-crossing at the same angular location ($\sim 40°$ with respect to the x-axis of the aberrated GSE coordinate system) at which MMS finally crossed the shock (the aberration angle is only 2.5°, considering planetary motion and the GSE x- and y-components of solar wind flow reported in the OMNI L1 data). The normalized model shock radius,
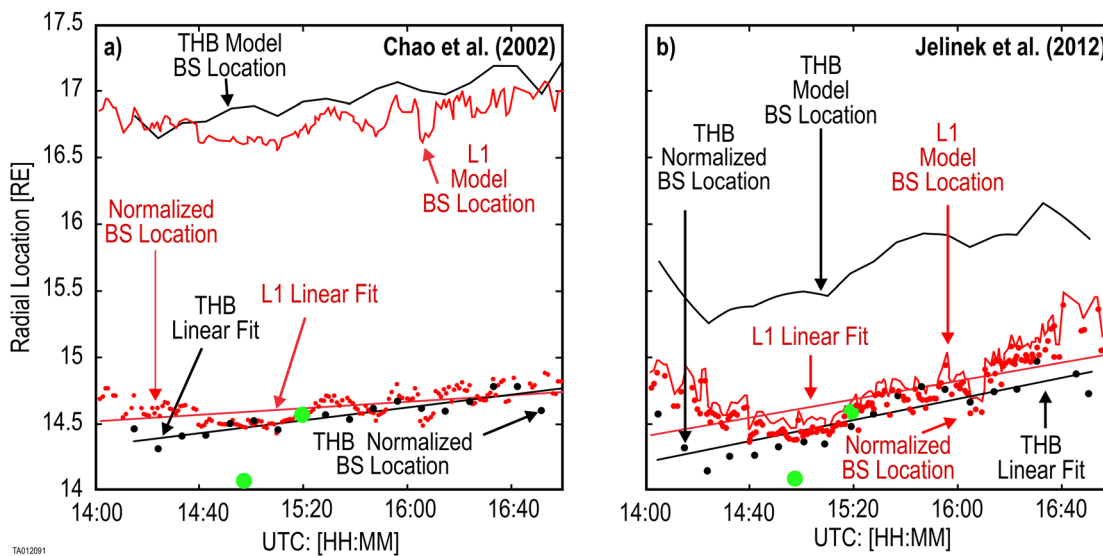

FIG. 4. MMS observing locations overplotted on the bow shock models of Chao *et al.* (2002) in the left panel (a) and Jelinek *et al.* (2012) in the right panel (b). The raw outputs of the models are presented as solid lines and outputs normalized to observed final crossing by MMS2 at the bottom as individual points. The model inputs use OMNI upstream data from L1 (red) and THEMIS-B data (black) from near (4, 58, −5) R_E, GSE. Linear fits to the normalized model results are shown as solid straight lines. Large green dots indicate the times and radial locations where MMS4 first encountered a solar wind-like stream just before 15:00 UTC and where MMS2 finally crossed the bow shock near 15:20 UTC. The diameters of these large green dots approximate the length of the MMS constellation against the y-axis.

R_{MN}, as driven by the L1 (red) and THEMIS-B (black) OMNI data are displayed as scatter plots in the lower portions of Fig. 4, along with similarly colored linear fits to the normalized data in each case. The residuals resulting from subtracting the normalized data from the linear fits form quasi-normal distributions with standard deviations in the case of the C02 model (panel a) of 0.093 (L1) and 0.067 R_E (THEMIS-B). By comparison, the standard deviations in the residuals from linear fitting to the J12 model (panel b) residuals are 0.18 (L1) and 0.13 R_E (THEMIS-B), roughly twice as large as the C02 results for both the L1 and THEMIS-B driving parameters. The large green dot located at (14:57:30 UTC, 14.07 R_E) is the point at which MMS4 observed the leading edge of the transient SW-like flow highlighted in Fig. 2. This is the most Earthward location at which this signature is observed and is 0.49 R_E closer to Earth than where the bow shock is finally crossed (large green dot, some 22 min later. Based on the C02 (J12) results, this is 5.3 (2.7) standard deviations in the cases of the L1 driving data and 7.3 (3.8) standard deviations in the cases of THEMIS-B driving data. We note here that neither the C02 or the J12 model is validated or intended to be applicable to either a Qpar shock or the near-parallel bow shock case highlighted in this study. Nor is either model intended to address smaller (non-global) bow shock features such as ripples or the pileup of finite-scale SLAMS as envisioned by Schwartz and Burgess (1991).

IV. DISCUSSION

Figure 1 demonstrates the known dominance exerted by the upstream SW and IMF over conditions in the magnetosheath. The transient event before 14:20 UTC and the enhanced fluxes at higher E/q thereafter [Fig. 1(b), vertical line 1] are coincident with the change of upstream magnetic geometry from Qprp to Qpar in this midmorning sector. The enhanced variability in virtually all shown MMS2 parameters [Figs. 1(a)–1(e)] and a greater tendency for the ion flow cone angle to exhibit excursions toward zero [Fig. 1(f)] are all associated with the IMF cone angle approaching zero, yielding near-parallelism of the IMF with the SW flow.

Several scenarios might explain the brief SW-like feature and bounding ULF magnetic structures observed near 14:57:40 UTC. A simple scenario involves a sequential global inward then outward motion of the bow shock such that the bow shock uniformly contracts, almost but not quite to the position of the inward-most spacecraft, MMS3, before expanding outward again. Surface waves traversing the bow shock, often referred to as ripples, have been shown [e.g., Johlander et al. (2016) and Gingell et al. (2017)] to account for spacecraft observations of repeated crossings of the shock from SW-like to magnetosheath-like plasma environments and back as the peaks and troughs of the bow shock surface wave pass over the spacecraft. These ripples have been cited as enabling the penetration of high-speed magnetosheath jets across the shock boundary and into the magnetosheath by Hietala and Plaschke (2013). Another plausible explanation is that, under these radial IMF conditions the bow shock surface, thought to be highly spatially and temporally structured on multiple scales under Qpar conditions (Schwartz and Burgess, 1991), exhibits an unusually deep localized incursion in this event, that is resolved in time and 1D space by MMS. Such an incursion might arise as a deficiency in the pileup of finite-scale blobs [or patches in the parlance and conceptual framework of Schwartz and Burgess (1991), Fig. 1]. In this case, a localized and temporary gap has formed. The likelihood of forming

such a gap would depend on the temporal and 3D spatial details of the patches and their accretion process.

In the case of any sequential in/out motion of the bow shock halting before reaching the trailing MMS3, leading-edge event features might be expected to pass over MMS2–1-4–3 in sequence during shock boundary contraction and in the opposite sequence (MMS3–4-1–2) with similar timing during expansion. Such a nested signature set is not observed. The event would also be less clear closer to Earth, as observed, owing to the halt of shock advance before reaching the trailing MMS3. Timing estimates based on ion flux spectrogram morphology (Fig. 2) indicate anti-sunward propagation at 10^2 km/s (Fig. 2, L1) at the leading edge and near simultaneity in termination of the SW-like ion fluxes in the trailing edge (Fig. 2, L2). Magnetic component feature timing suggests near 10^2 km/s Earthward propagation along the line of the MMS constellation at both leading and trailing event edges. Furthermore, the duration of the event, based on processed bounding ULF-like GSE By (Fig. 3), is remarkably constant in time across spacecraft at near 58 s duration. Given the upstream solar wind speed, near 375 km/s, if the disturbance were caused by a plasma structure (e.g., a foreshock caviton) of finite extent in the GSE-x direction impinging on the bow shock, this duration would correspond to an extent of 3.4 Earth radii, very near the peak of the caviton size distribution shown in Fig. 8 of Kajdič et al. (2013). This event, bounded on leading and trailing edges by steepened left-hand polarized (spacecraft frame) ULF waves and containing reduced magnetic field and density as well as (some) more energetic particles but no ULF waves, is indeed reminiscent of foreshock cavitons described by Blanco-Cano et al. (2009), except that foreshock cavitons are an upstream phenomenon, with density and magnetic depressions relative to the background foreshock values. If our observations are related to such cavitons, then the question of how the structure comes to reside so far inside the magnetosheath requires consideration. The observations reported here are distinct from the magnetosheath cavities studied by Katırcıoğlu et al. (2009), which are typically characterized by local decrease in magnetosheath bulk flow speed, unlike the high-speed solar wind-like stream reported here.

Comparison of the variability in the normalized bow shock model results with the most Earthward observation of SW-like high-speed plasma flow at MMS4 demonstrates that it is unlikely that global SW conditions measured either at L1 or much closer to Earth by THEMIS-B drive a global bow shock contraction sufficient to be observed by MMS near 14:57 UTC, given the shock location at the time of final shock crossing by MMS2 at 15:19:35 UTC. However, this depth of penetration is consistent with the scales (around 40 ion inertial lengths) found in magnetosheath jet-like features in local 2D hybrid simulation results reported by Hao et al. (2016) (Fig. 5 of that work) and is also within the range of distances from the bowshock within which the simulation results of Tinoco-Arennas et al. (2022) found a relative abundance of magnetosheath jets. Nevertheless, a noteworthy difference between the observations here and those of the Hao et al. (2016) simulation results is that, while the simulation has the high-speed jet localized to and aligned with regions of the strongest magnetic field, the high-speed ion flow shown here in Fig. 2 is accompanied by minimal magnetic intensity as in the pristine SW. Raptis et al. (2022), interpreting the trailing edge of the event in Fig. 2 as an example of local bow shock reformation, demonstrate the operation of the shock reformation process to produce a magnetosheath jet at

MMS3 at 14:57:34 UTC, within the event of Fig. 2 shown here. The jet described in that work is at substantially smaller scale in both time and space than the minute-long high-speed flow (in the SC frame at MMS2) that is the focus of this report and that forms the environment in which the jet reported there is formed. Furthermore, the jet reported by Raptis et al. satisfies the enhanced dynamic pressure criterion typically used in other works [see, e.g., Plaschke et al. (2018) and Archer and Horbury (2013)] for categorization as a magnetosheath jet, while the event highlighted in Fig. 2 of this study does not satisfy this criterion. In contrast, we focus here on the questions of (1) how the observed shock structure comes to be located so far Earthward of the later-observed final shock crossing, in view of measured conditions in the external SW? and (2) what can this tell us about mesoscale (smaller than those of the global bow shock but larger than local kinetic scales) shock structuring under these near-radial IMF conditions? The event described in the present paper is unlike magnetosheath jets reported in the literature, which are composed of shocked (magnetosheath-like) plasma, in contrast to the SW-like high Mach number plasma in the event reported here.

Propagating bow shock ripples, like those predicted under Qprp conditions in hybrid simulations by Lowe and Burgess (2003), has now been observed at high 3D spatial resolution by both Johlander et al. (2016) and Gingell et al. (2017). In both cases, the MMS constellation was in tetrahedral formation of length scale smaller than the ion inertial length (λ_i). Johlander et al. (2016) observations were obtained under Qprp conditions, while those of Gingell et al. (2017) were obtained under marginally Qpar ($\theta_{Bn} \sim 45°$) geometry. Both studies reported ripple wavelengths of a few λ_i and spatial ripple amplitudes less than or on the order of λ_i, consistent with previous (Lowe and Burgess, 2003) and concurrent [Gingell et al. (2017)] hybrid simulations. Thus, bow shock ripples as envisioned by Lowe and Burgess (2003) and Johlander et al. (2016) are not a plausible explanation for the observations presented here. In contrast, Hietala et al. (2009) reported a bow shock "ripple" observed under Qpar conditions with the Cluster spacecraft constellation. They inferred a spatial scale of 1–3 Earth radii and cite a lower limit of 8000 km ($\sim$50 λ_i). Though the authors do not differentiate between wavelength and spatial amplitude, the sketch in Fig. 3 shows them about the same. This larger scale is similar to both the scale of the linear MMS constellation and the distance between the observations featured here in Fig. 2 and the later final bow shock crossing. A feature with such a scale and propagating tangential to the nominal bow shock surface could indeed yield a signature similar to that reported here. Furthermore, the simulation study by Kajdič et al. (2021), yields an estimate of only 20 λ_i for the amplitude of the largest ripples in their "strongly rippled" bow shock, roughly half of what would be required for a shock ripple to account for the observations presented in this study. Finally, undulations like those observed by Krauss-Varban (2008) in hybrid simulations of an interplanetary shock are also larger scale phenomena (approximately 100 λ_i), though the existence, coherence, or spatial amplitude of such undulations on Earth's bow shock surface are unknown.

If global contraction/expansion is not the cause of the MMS observations presented in Fig. 2, then a more local phenomenon must be involved. It is possible and plausible that some foreshock disturbance with transverse dimensions smaller than the distance at the time between Earth and the THEMIS-B observation point causes contraction of the shock surface. Such a disturbance at the large end of this

scale range would also be global from the point of view of Earth's bow shock. Upstream ion cyclotron or ion inertial scales, both in the range 10^2–10^3 km and therefore local on Earth's bow shock scales, likely limit the size at the small end of the scale. An alternative explanation is that dynamic processes at the Qpar bow shock itself enable the shock surface to exist locally at radial locations not predicted by the model in use. This might involve a combination of phenomena (contraction/expansion, shock reformation, traveling surface wave) enabling penetration to our observation point or assimilation of a mesoscale sized structure like that reported here. Such processes would be limited at large-scale by the size of the bow shock Qpar region and on the small scale by the characteristic upstream ion lengths. These considerations raise the question: if local scale structuring of the bow shock exists, then what are the structures and dynamics associated with their boundaries?

In the conceptual context of the Qpar bow shock as a "patchwork of three-dimensional structures" (Schwartz and Burgess, 1991), the observations presented here might represent an interstitial element of three-dimensional space between the patches that has survived, unshocked, to the place in space and time reported here. Inspection of their Fig. 1, with the increasing density of "patches" toward the left (nominal shock surface) gives the impression that the survival of such an interstitial volume to the depth reported in this study is statistically highly unlikely if the size of that volume is of the same or larger scale as that of the patches, though the cartoon nature of the illustration needs to be borne in mind when considering this impression. This scenario, or one in which the MMS spacecraft flew through a deep and spatially localized undulation in the shock surface, seem the most promising concepts in attempting to understand these observations.

The dispersed properties in both magnetic and ion flux signatures at the event leading edge and of the magnetic signatures only on the trailing edge are perplexing. The magnetic wave evidently consistently propagates anti-sunward as shown both by time dispersion and consistent magnetic polarization in the spacecraft frame. The simultaneity in the morphological ion boundary (L2 in Fig. 2) might indicate an arbitrary oriented, very high-speed front or, more likely, a front oriented nearly parallel to the linear spacecraft array. There are examples of highly structured shock boundaries under quasi-radial bow shock conditions found in 3D hybrid simulations of Chen et al. (2021) and Ng et al. (2021) and the 2D hybrid Vlasov simulations of Johlander et al. (2022). The work of Johlander et al. (2022) compared MMS data (closely spaced tetrahedral formation for their event) at the Qpar bow shock with a hybrid simulation. Their simulation (see their Fig. 3) could produce timing signatures similar to those we observe in the ion spectrogram morphology near L2 in Fig. 2.

An outstanding question is, why would we see different timing signatures in the ion spectrogram morphology than we do in the magnetic signatures on the trailing edge? Future studies may reveal whether this feature is common or significant, a topic beyond the scope of the present study.

Finally, the low-amplitude, higher-frequency, right-hand polarized (in the spacecraft frame) wave train observed in the magnetic components most prominently at MMS2 [see Fig. 2(a)] between 14:57:20 and 14:57:55 UTC is likely composed of whistler waves that are typically observed on the upstream side of a SLAMS (Schwartz et al., 1992). These waves display an interesting frequency shift near the middle of the event, such that the SC-frame frequency is higher

(near 1.2 Hz) early in the event and lower (near 0.7 Hz) later. Such a signature is consistent with a wave source moving toward the observer and then receding. For an omnidirectional source, that motion might consist of either: (a) approach and then reverse direction to recede or (b) approach, reach its closest approach, and then continue onward, receding.

V. CONCLUSIONS

In this work, we reveal a magnetosheath that exhibits several types of evolution, all dominantly driven by the state of the upstream IMF or changes in that state. First, in response to a large-scale IMF transition, the shock magnetic geometry upstream of MMS changes from Qprp to Qpar with corresponding changes in the magnetosheath at MMS, including enhanced magnetic fluctuations and the appearance of superthermal ions. As the IMF becomes almost purely radial, a SW-like anti-sunward flowing ion signature, featuring small $|\mathbf{B}|$ as in the SW, appears as an isolated event in the time series of otherwise magnetosheath-like plasma and magnetic field. This event is observed approximately 3000 km (about 40 λ_i, based on an upstream ion density of $10 \, cm^{-3}$) anti-sunward of where the bow shock is finally crossed 22 min later. The leading edge of both the magnetic and ion flux signatures along the linear MMS constellation is dispersed among the four MMS spacecraft, indicating an anti-sunward propagation speed along the constellation line of near10^2 km/s. The trailing edge signature is dispersed in the same sense, considering only the magnetic component signatures, though a chosen marker in the ion flux signatures indicates a high degree of simultaneity among the spacecraft. In no case is the dispersion observed to reverse as might be expected for a rigidly contracting and then expanding bow shock. Furthermore, there is no indication in the results of the Chao et al. (2002) bow shock model that the variability in the SW and IMF measured both at L1 and nearer Earth in cis-lunar orbit, is sufficient to contract the bow shock to the radial location (14.08 RE) observed by MMS4 at 14:57:25 UTC, given its radial location (14.56 R_E) when MMS2 finally crossed into the SW at 15:19:35 UTC. This is supported, though less conclusively, by a similar analysis using a second (Jelinek, 2012) shock model. From the observations and model results described here, we conclude the following:

(1) An extended high-speed SW-like ion flow with magnetic and ion properties that are similar to the upstream environment is seen to penetrate a large fraction of an Earth radius beyond the location where the bow shock is finally crossed, 22 min later.

(2) The high-speed flow region ion flux and magnetic characteristics are observed most clearly closest to the nominal bow shock (MMS2) and progressively less clearly at the larger distances of MMS1, MMS4, and then MMS3 where it is finally difficult to recognize.

(3) The high-speed flow region is bounded on its leading and trailing edges by strong cyclic magnetic field variations dominant in GSE By and Bz, indicating approximately circularly polarized ULF waves known to evolve into SLAMS and pile up as at the Qpar shock.

(4) Dispersion in the timing of magnetic and ion flux signatures along the string-of-pearls MMS spacecraft constellation indicates approximate10^2 km/s earthward propagation at its leading edge. Trailing edge signatures indicate similar or smaller time dispersion along the line of the MMS constellation. In no case does the dispersion reverse, undermining interpretation of the observations as a simple rigid contraction/expansion cycle at similar rates.

(5) Quantitative analysis of the variability in upstream parameters that determine bow shock location, measured both at L1 and much closer to Earth at cis-lunar orbit, show that variability is insufficient to drive the shock to the location where SW-like flows are observed by MMS4, given the location of final shock crossing 22 min later by MMS2. This further undermines a simple externally driven rigid contraction/expansion cycle.

(6) Bow shock ripples are a plausible explanation for the observations reported here, though most reports of observed or simulated bow shock ripples have insufficient amplitude.

(7) Magnetic signatures plausibly common across each element of the linear MMS constellation demonstrate a common event time scale near 58 s.

(8) At least three similar but less clear and shorter duration events within the same 3-min interval under study are identified.

(9) Higher frequency (near 1 Hz in spacecraft frame) waves observed during the high-speed flow interval at MMS2 are seen to undergo a frequency shift consistent with a sequentially approaching and then receding Doppler-shifted source at some intermediate frequency.

Full interpretation of the observations presented here remains ambiguous. An interpretation in terms of a highly and dynamically corrugated shock surface is consistent with these observations, while interpretation in terms of a sequential quasi-rigid contraction/expansion cycle is not, owing primarily to (1) absence of the nested signature expected from a sequential expansion/contraction cycle and (2) the observed lack of sufficient variability in the upstream parameters that control nominal shock location to account for the disparity of nearly 0.5 R_E between final shock crossing by MMS2 and the deepest penetration of the high-speed ion flow observed by MMS4. The bow shock and magnetosheath are highly dynamic and structured during quasi-radial IMF. Global 3D and 2D Vlasov simulations indicate that the magnetosheath can be fragmented with deep troughs due to foreshock waves and turbulence, a feature captured by the MMS measurements reported in this study.

SUPPLEMENTARY MATERIAL

See the supplementary material for the further details of the timing of in the ion flux feature described in the context of Fig. 2 can be found in supplementary material S1.

AUTHOR DECLARATIONS
Conflict of Interest

The authors have no conflicts to disclose.

Author Contributions

Craig J. Pollock: Conceptualization (equal); Formal analysis (equal); Investigation (equal); Methodology (equal); Software (equal); Writing – original draft (equal); Writing – review & editing (equal). **Christopher Thomas Russell:** Conceptualization (equal); Investigation (equal). **Li-Jen Chen:** Conceptualization (supporting); Writing – original draft (supporting). **Steve Schwartz:** Conceptualization (supporting); Writing – review & editing (supporting). **Shan Wang:** Methodology (supporting); Writing – review & editing (supporting). **Levon A. Avanov:** Investigation (equal); Writing – review & editing (supporting). **James Leo Burch:** Conceptualization (supporting); Data curation (lead); Funding acquisition (lead); Investigation (equal); Resources (lead); Supervision (supporting). **Daniel J. Gershman:** Data curation (equal); Investigation (equal); Project administration (lead); Software (supporting). **Barbara L. Giles:** Data curation (equal); Funding acquisition (equal); Investigation (equal); Software (equal). **Savvas Raptis:** Writing – review & editing (equal).

DATA AVAILABILITY

Level 2 OMNI data used in this study were generated from raw spacecraft data at NASA's Goddard Space Flight Center Space Physics Data Facility and raw level 2 data used in this study were generated from raw spacecraft data at the University of Colorado, Laboratory for Atmospheric and Space Physics MMS Science Data Center. Derived data supporting the findings of this study are available from the corresponding author upon reasonable request.

REFERENCES

Angelopoulos, V., "The ARTEMIS mission," Space Sci. Rev. **165**, 3–25 (2011).

Archer, M. O. and Horbury, T. S., "Magnetosheath dynamic pressure enhancements: Occurrence and typical properties," Ann. Geophys. **31**, 319–331 (2013).

Auster, H. U., Glassmeier, K. H., Magnes, W., Aydogar, O., Baumjohann, W., Constantinescu, D., Fischer, D., Fornacon, K. H., Georgescu, E., Harvey, P. et al., "The THEMIS fluxgate magnetometer," Space Sci. Rev. **141**(1–4), 235–264 (2008).

Bale, S. D., Mozer, F. S., and Horbury, T. S., "Density-transition scale at quasiperpendicular collisionless shocks," Phys. Rev. Lett. **91**, 265004 (2003).

Blanco-Cano, X., Omidi, N., and Russell, C. T., "Global hybrid simulations: Foreshock waves and cavitons under radial interplanetary magnetic field geometry," J. Geophys. Res. **114**, A01216, https://doi.org/10.1029/2008JA013406 (2009).

Burch, J. L., Moore, T. E., Torbert, R. B., and Giles, B. L., "Magnetospheric multiscale overview and science objectives," Space Sci. Rev. **199**, 5–21 (2016).

Burgess, D., "Cyclic behavior at quasi-parallel collisionless shocks," Geophys. Res. Lett. **16**(5), 345–348, https://doi.org/10.1029/GL016i005p00345 (1989).

Burgess, D., "Collisionless shocks," in Introduction to Space Physics, edited by M. G. Kivelson and C. T. Russell (Cambridge University Press, 1995).

Chao, J. K., Wu, D. J., Lin, C.-H., Yang, Y.-H., Wang, X. Y., Kessel, M., Chen, S. H., and Lepping, R. P., "Models for the size and shape of the Earth's magnetopause and bow shock," COSPAR Colloq. Ser. **12**, 127–135 (2002).

Chen, L.-J., Ng, J., Omelchenko, Y., and Wang, S., "Magnetopause reconnection and indents induced by foreshock turbulence," Geophys. Res. Lett. **48**, e2021GL093029, https://doi.org/10.1029/2021GL093029 (2021).

Gingell, I., Schwartz, S. J., Burgess, D., Johlander, A., Russell, C. T., Burch, J. L., Ergun, R. E., Fuselier, S., Gershman, D. J., Giles, B. L. et al., "MMS observations and hybrid simulations of surface ripples at a marginally quasi-parallel shock," J. Geophys. Res. **122**, 11003–11017, https://doi.org/10.1002/2017JA024538 (2017).

Hao, Y., Lembege, B., Lu, Q., and Guo, F., "Formation of downstream high-speed jets by a rippled nonstationary quasi-parallel shock: 2D hybrid simulations," J. Geophys. Res. **121**, 2080–2094, https://doi.org/10.1002/2015JA021419 (2016).

Hietala, H., Laitinen, T. V., Andreeova, K., Vainio, R., Vaivads, A., Palmroth, M., Pulkkinen, T. I., Koskinen, H. E. J., Lucek E. A., and Rème H., "Supermagnetosonic jets behind a collisionless quasiparallel shock," Phys. Rev. Lett. **103**, 245001 (2009).

Hietala, H. and Plaschke, F. J., "On the generation of magnetosheath high-speed jets by bow shock ripples," J. Geophys. Res. Space Phys. **118**(11), 7237–7245, https://doi.org/10.1002/2013JA019172 (2013).

Jelinek, K., Nemecek, Z., and Safrankova, J., "A new approach to magnetopause and bow shock modeling based on automated region identification," J. Geophys. Res. **117**, A05208, https://doi.org/10.1029/2011JA017252 (2012).

Johlander, A., Battarbee, M., Turc, L., Ganse, U., Pfau-Kemph, Y., Gandin, M., Suni, J., Tarvus, V., Bussov, M., Zhou, H. et al., "Quasi-parallel shock reformation seen by magnetospheric mulitscale and ion-kinetic simulations," Geophys. Res. Lett. **49**, e2021GL096335, https://doi.org/10.1029/2021GL096335 (2022).

Johlander, A., Schwartz, S. J., Vaivads, A., Khotyaintsev, Y. V., Gingell, I., Peng, I. B., Markidis, S., Lindqvist, P.-A., Ergun, R. E., Marklund, G. T. et al., "Rippled quasiperpendicular shock observed by magnetospheric multiscale spacecraft," Phys. Rev. Lett. **117**, 165101 (2016).

Kajdič, P., Blanco-Cano, X., Omidi, N., Meziane, K., Russell, C. T., Sauvaud, J.-A., Dandouras, I., and Lavraud, B., "Statistical study of foreshock cavitons," Ann. Geophys. **31**, 2163–2179 (2013).

Kajdič, P., Pfau-Kempf, Y., Turc, L., Dimmock, A. P., Palmroth, M., Takahashi, K., Kilpua, E., Soucek, J., Takahashi, N., Preisser, L. et al., "ULF wave transmission across collisionless shocks: 2.5D local hybrid simulations," J. Geophys. Res. **126**, e2021JA029283, https://doi.org/10.1029/2021JA029283 (2021).

Karimabadi, H., Roytershteyn, V., Vu, H. X., Omelchenko, Y. A., Scudder, J., Daughton, W., Dimmock, A., Nykyri, K., Wan, M., Sibeck, D., Tatineni, M., Majumdar, A., Loring, B., and Geveci, B., "The link between shocks, turbulence, and magnetic reconnection in collisionless plasmas," Phys. Plasmas **21**, 062308 (2014).

Katırcıoğlu, F. T., Kaymaz, Z., Sibeck, D. G., and Dandouras, I., "Magnetosheath cavities: Case studies using Cluster observations," Ann. Geophys. **27**, 3765–3780 (2009).

Krauss-Varban, D., Li, Y., Luhmann, J. G. et al., "Ion acceleration at the earth's bow shock and at interplanetary shocks: A comparison," in Particle Acceleration and Transport in the Heliosphere and Beyond: 7th Annual Astrophysics Conference, edited by G. Li (AIP, 2008), pp. 307–313.

Krauss-Varban, D., Pantellini, F. G. E., and Burgess, D., "Electron dynamics and whistler waves at quasi-perpendicular shocks," Geophys. Res. Lett. **22**, 2091–2094, https://doi.org/10.1029/95GL01782 (1995).

Lepping, R. P., Acūna, M. H., Burlaga, L. F., Farrrell, W. M., Slavin, J. A., Schatten, K. H., Mariani, F., Ness, N. F., Neubauer, F. M., Whang, Y. C. et al., "The WIND magnetic field investigation," Space Sci. Rev. **71**, 207–229 (1995).

Liu, T. Z., Hao, Y., Wilson, L. B., Turner, D., and Zhang, H., "Magnetospheric multiscale observations of Earth's oblique bow shock reformation by foreshock ultralow-frequency waves," Geophys. Res. Lett. **48**(2), e2020GL091184, https://doi.org/10.1029/2020GL091184 (2021).

Lowe, R. E. and Burgess, D., "The properties and causes of rippling in quasi-perpendicular collisionless shock fronts," Ann. Geophys. **21**, 671–679 (2003).

Lucek, E. A., Horbury, T. S., Dandouras, I., and Reme, H., "Cluster observations of the Earth's quasi-parallel bow shock," J. Geophys. Res. **133**(A7), 012756, https://doi.org/10.1029/2007JA012756 (2008).

McComas, D., Bame, S., Barker, P., Feldman, W. C., Phillips, J. L., Riley, P., and Griffe, J. W., "Solar wind electron proton alpha monitor (SWEPAM) for the advanced composition explorer," Space Sci. Rev. **86**, 563–612 (1998).

McFadden, J. P., Carlson, C. W., Larson, D., Ludlam, M., Abiad, R., Elliott, B., Turin, P., Marckwordt, M., and Angelopoulos, V., "The THEMIS ESA plasma instrument and in-flight calibration," Space Sci. Rev. **141**, 277 (2008).

Ng, J., Chen, L.-J., and Omelchenko, Y. A., "Bursty magnetic reconnection at the Earth's magnetopause triggered by high-speed jets," Phys. Plasmas **28**, 092902 (2021).

Ogilvie, K. W., Chornay, D. J., Fritzenreiter, R. J., Hunsaker, F., Keller, J., Lobell, J., Mille, G., Scudder, J. D., Sittler, E. C., Torbert, R. B. et al., "SWE, a comprehensive plasma instrument for the WIND spacecraft," Space Sci. Rev. **71**, 55–77 (1995).

Plaschke, F., Hietala, H., Archer, M., Blanco-Cano, X., Kajdic, P., Karlsson, T., Lee, S. H., Omidi, N., Palmroth, M., Roytershteyn, V. *et al.*, "Jets downstream of collisionless shocks," Space Sci. Rev. **214**, 1–77 (2018).

Pollock, C., Moore, T., Jacques, A., Burch, J., Gliese, U., Saito, Y., Omoto, T., Avanov, L., Barrie, A., Coffey, V. *et al.*, "Fast plasma investigation for magnetospheric multiscale," Space Sci. Rev. **199**, 331–406 (2016).

Raptis, S., Karlsson, T., Vaivads, A., Pollock, C., Plaschke, F., Johlander, A., Trollvik, H., and Lindqvist, P.-A., "Downstream high-speed plasma jet generation as a direct consequence of shock reformation," Nat. Commun. **13**, 598 (2022).

Russell, C. T., Anderson, B. J., Baumjohann, W., Bromund, K. R., Dearborn, D., Fischer, D., Le, G., Leinweber, H. K., Leneman, D., Magnes W. *et al.*, "The magnetospheric multiscale magnetometers," Space Sci. Rev. **199**, 189–256 (2016).

Schwartz, S. J. and Burgess, D., "Quasi-parallel shocks: A patchwork of three-dimensional structures," Geophys. Res. Lett. **18**, 373–376, https://doi.org/10.1029/91GL00138 (1991).

Schwartz, S. J., Burgess, D., Wilkinson, W. P., Kessel, R. L., Dunlop, M., and Luhr, H., "Observations of short large-amplitude magnetic structures at a quasi-parallel shock," J. Geophys. Res. **97**(A4), 4209–4227, https://doi.org/10.1029/91JA02581 (1992).

Smith, C. W., L'Heureux, J. L., Ness, N. F., Acuna, M., Burlaga, L. F., and Scheifele, J., "The ACE magnetic fields experiment," Space Sci. Rev. **86**(1), 613–632 (1998).

Tinoco-Arenas, A., Kajdic, P., Preisser, L., Blanco-Cano, X., Trotta, D., and Burgess, D., "Parametric study of magnetosheath jets in 2D local hybrid simulations," Front. Astron. Space Sci. **9**, 793195 (2022).

Torbert, R. B., Russell, C. T., Magnes, W., Ergun, R. E., Lindqvist, P.-A., LeContel, O., Vaith, H., Macri, J., Meyers, S., Rau, D. *et al.*, "The FIELDS instrument suite on MMS: Scientific objectives, measurements, and data products," Space Sci. Rev. **199**, 105–135 (2016).

Winske, D. and Quest, K. B., "Magnetic field and density fluctuations at perpendicular supercritical collisionless shocks," J. Geophys. Res. **93**, 9681–9693, https://doi.org/10.1029/JA093iA09p09681 (1988).